Journal of Fluids and Structures 127 (2024) 104124

Contents lists available at ScienceDirect

Journal of Fluids and Structures

journal homepage: www.elsevier.com/locate/jfs

Experimental investigation of rear flexible flaps interacting with the wake dynamics behind a squareback Ahmed body

J.C. Muñoz-Hervás [a,b], M. Lorite-Díez [b,c,*], C. García-Baena [b,c], J.I. Jiménez-González [a,b]

[a] Departamento de Ingeniería Mecánica y Minera. Universidad de Jaén, Campus de las Lagunillas, 23071, Jaén, Spain
[b] Instituto Interuniversitario de Investigación del Sistema Tierra en Andalucía. Universidades de Granada, Jaén, Córdoba, Spain
[c] Departamento de Mecánica de Estructuras e Ingeniería Hidráulica. Universidad de Granada, Campus de Fuentenueva, 18071, Granada, Spain

ARTICLE INFO

Keywords:
Turbulent wakes
Ahmed body
Fluid–structure interaction
Flow induced vibrations
Experimental fluid mechanics

ABSTRACT

We have conducted an experimental study on the use of rear flexible vertical flaps as adaptive solutions to reduce the drag of a squareback Ahmed body, and on the fluid–structure interaction mechanisms at the turbulent wake. To that aim, wind tunnel experiments were conducted to compare the performance of various configurations including the baseline body, the body with rigid flaps and with flexible flaps. These configurations were tested under different aligned and cross-flow conditions. The results reveal that the flexible adaptive devices effectively reduce the drag within for low values of the dimensionless stiffness quantified through the Cauchy number, Ca. Thus, the two-dimensional deformation of the flexible flaps, which undergo progressive inwards reconfiguration (with an averaged tip deflection angle of $\Theta \simeq 4°$), reduces the bluffness of the flow separation at the body base, thus shrinking the recirculation region. This reconfiguration leads to increased base pressure, resulting into a 8.3% decrease in the global drag, C_D, under aligned conditions. Similar drag reductions are observed under yawed conditions.

Two regimes are identified in terms of the coupled fluid–structure dynamics. For low Ca, the passive reconfiguration of the flaps include small amplitude, periodic oscillations corresponding to the first free deformation mode of a cantilevered beam. Alongside these weak oscillations, the flaps are deformed guided by the changes in the value of the horizontal base pressure gradient, depicting bi-stable behavior which is caused by the synchronization between the Reflectional Symmetry Breaking (RSB) mode, typically present in the wake of three-dimensional bluff bodies, and the flaps deformation. For higher values of Ca, the flexible flaps deflect inwardly by about $\Theta \simeq 20°$ on average, but exhibit vigorous oscillations combining the first and second free deformation modes of a cantilevered beam. These large amplitude oscillations excite the flow separation at the model's trailing edges, leading to significant fluctuations in the separated shear layers and a consequent 31% increase in the global drag. Under yawed conditions, the flaps responses for large values of Ca are different due to the asymmetry of the corresponding recirculation region.

1. Introduction

Transportation industry accounts for 30% of greenhouse gas emissions in the EU, with trucks and buses contributing a quarter of that figure (European Environment Agency, 2021). Due to specific requirements regarding load capacity, docking, and driving

* Corresponding author at: Instituto Interuniversitario de Investigación del Sistema Tierra en Andalucía. Universidades de Granada, Jaén, Córdoba, Spain.
E-mail address: mldiez@ugr.es (M. Lorite-Díez).

https://doi.org/10.1016/j.jfluidstructs.2024.104124
Received 30 September 2023; Received in revised form 2 March 2024; Accepted 10 April 2024
Available online 4 May 2024
0889-9746/© 2024 The Author(s). Published by Elsevier Ltd. This is an open access article under the CC BY license (http://creativecommons.org/licenses/by/4.0/).

conditions, trucks and buses stand out as significant energy consumers and environmental pollutants within the EU road transport sector (European Environment Agency, 2021). A substantial portion of their fuel consumption and associated greenhouse gas emissions, particularly CO_2, can be attributed to their aerodynamically inefficient design. Medium and heavy trucks, commonly operating on highways, expend up to 70% of their energy combating aerodynamic drag (National Research Council, 2010), with approximately 25% of this drag stemming from the rear portion of the truck (Wood and Bauer, 2003).

The blunt shape of trucks leads to massive airflow separation at their trailing edges, creating turbulent, three-dimensional wakes characterized by recirculating regions and low-pressure zones. Academic studies often employ simplified models such as the Ahmed (Ahmed et al., 1984), Windsor (Howell et al., 2013) or GTS (Gutierrez et al., 1995) bodies to investigate fundamental aspects of heavy vehicle aerodynamics (Ahmed et al., 1984). These models retain key features of the rear flow on heavy vehicles (Choi et al., 2014), enabling fundamental research aimed to develop efficient drag reduction strategies.

This study focuses on the square-back Ahmed body, extensively analyzed in previous research works such as Duell and George (1999), Khalighi et al. (2001), Grandemange et al. (2013a,b) and Haffner et al. (2020). The wake behind this model exhibits various unsteady phenomena, including vortex shedding, recirculation bubble pumping, and the Reflectional-Symmetric-Breaking (RSB) mode, which induce quasi-static switching between asymmetric wake deflected states (Grandemange et al., 2013b). This mode, also observed in other simplified models and axisymmetric bodies, generate side forces that impact drag (Bonnavion and Cadot, 2018). Moreover, given that heavy vehicles often encounter crosswind conditions, the study of their wakes under yawed conditions is crucial (Hucho and Sovran, 1993). In particular, McArthur et al. (2018) described the appearance of streamwise vortices at the model longitudinal edges under yawed conditions, contributing importantly to recirculation region pressure level, and therefore, to the aerodynamic drag of the Ahmed body. Globally, the effect of all these flow features on the aerodynamic drag is captured by the pressure distribution at the body base (Evrard et al., 2016; Lorite-Díez et al., 2020a) and it is usually related to changes in the length and width of the recirculation region behind the tested model (Lorite-Díez et al., 2020b).

To mitigate the aerodynamic drag of heavy vehicles, various rear passive devices have been proposed in the literature, including rigid cavities (Khalighi et al., 2001; Choi et al., 2014; Grandemange et al., 2015; Evrard et al., 2016) or flaps (García de la Cruz et al., 2017; Varney et al., 2018; Urquhart et al., 2021) among others. These devices are able to manipulate the flow separation, reducing the recirculation region bluffness or increasing the recirculation length, recovering base pressure and consequently, reducing the aerodynamic drag. Nevertheless, the performance of these devices depends on the flow alignment as reported, e.g. by Lorite-Díez et al. (2020a) who showed that the aerodynamic efficiency of a straight cavity is considerably reduced at yawed conditions. Therefore, the use of self-adaptive systems may constitute an appealing approach, as the flaps may reconfigure to different flow orientations. Following this idea, flexibly-hinged flaps have shown promising results in adapting to changing flow conditions and optimizing drag reduction (García-Baena et al., 2023; Camacho-Sánchez et al., 2023) for, respectively, two and three-dimensional blunt bodies.

In this regard, flexible appendages have been tested in various flow scenarios, including wake control of a fixed cylinder (Kunze and Brücker, 2012; Abdi et al., 2019; Mao et al., 2022), attenuation of vortex-induced vibrations of an elastically mounted cylinder (Cui et al., 2022), and drag reduction of two-dimensional D-shaped blunt bodies (García-Baena et al., 2021a,b). These studies, exploring different degrees of freedom, demonstrate the ability of rear flexible flaps to render the rear flow separation more aerodynamic, and therefore, decreasing the drag. Furthermore, these devices exhibit different mechanisms of fluid–structure interaction as quasi-static passive deformation, frequency and phase locking between flaps deformation and wake dynamics or the emergence of different vibration modes. However, examples of employing flexible flaps in the wake of three-dimensional heavy vehicle models, such as the square-back Ahmed body, remain scarce.

Therefore, this study aims to investigate the aerodynamic effects of rear flexible flaps on a square-back Ahmed body under both aligned and crossflow conditions, while also exploring the relationship between flap deformation and wake dynamics. That said, the paper is organized as follows: the experimental set-up is described in Section 2, followed by the presentation and discussion of results in Section 3 through subsequent sections, focusing on base flow characterization in Section 3.1, drag reduction in Section 3.2, flap deformation in Section 3.3, and wake-flap interaction in Section 3.4. Finally, the main conclusions are drawn in Section Section 4.

2. Experimental set-up

We studied experimentally the wake behind a square-back Ahmed body of height $H = 72$ mm, length $L = 4.04H$, and width $W = 1.35H$ (see Fig. 1a), placed inside a recirculating wind tunnel available at the University of Jaén, with a nozzle of 8:1 contraction ratio connected to a 400×500 mm^2 test section. The wind tunnel allows a variation of the free-stream velocity in the test section between 5 and 20 m/s, with a turbulent intensity below 1%. Furthermore, the flow uniformity along the test section is better than 98% for the selected range of wind velocities. The model was placed at a ground clearance of $c/H = 0.27$. The coordinate system origin is set at the center of the Ahmed body base, with x being the direction perpendicular to the body base, z the vertical direction, and y the direction that forms a right-hand trihedron. The experimental facility allows precise setting of the orientation between the main body axis and the incoming wind, using an automatized rotation stage. Thus, three different values of the yaw angle, $\beta = 0°, 5°, 10°$, were tested. In order to find the aligned condition between the body and the incoming wind, we sought, for the baseline case, a symmetrical distribution of the RSB mode to compensate any asymmetry in our experimental facility, as done in Evrard et al. (2016).

We used two flexible brass foils of length $B = 0.46H$ and calibrated thickness $e/H = 3.5 \cdot 10^{-4}$. Those foils, embedded at the base edges, acted as cantilevered flaps when subjected to the flow around the square-back Ahmed body. The selection of these flaps was the result of an initial parametric study varying flaps materials, thickness, and lengths that allowed us to observe a valid adaptive

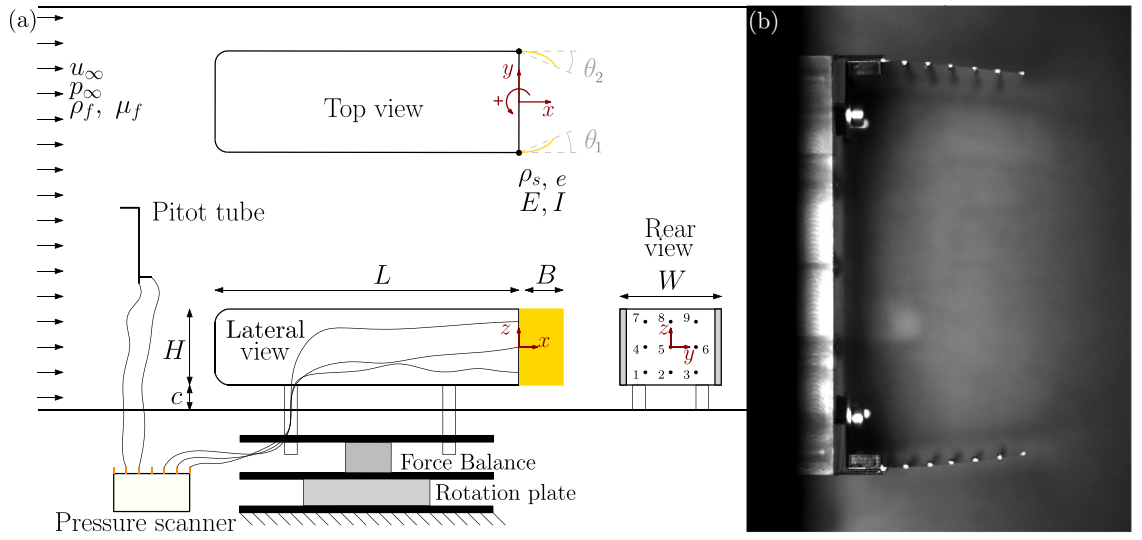

Fig. 1. (a) Sketch of the experimental set-up. (b) Illustration of the instantaneous deflection of the flexible flaps at $Re \simeq 77000$ ($Ca \simeq 43$).

Table 1
Definition and ranges from the main variables of the fluid–structure interaction problem.

Main parameters	Symbol	Definition	Range
Reynolds number	Re	$\frac{\rho_f u_\infty H}{\mu_f}$	(48000, 87000)
Mass ratio	m^*	$\frac{\rho_s}{\rho_f}$	7000
Reduced velocity	U^*	$\frac{u_\infty}{f_n H}$	[10.7, 19]
Cauchy number	Ca	$\frac{\rho_f u_\infty^2 H B^3}{2EI}$	[16.8, 53.2]
Mass damping ratio	ξm^*	–	167
Yaw angle	β (deg.)	–	0°, 5°, 10°
Angular flap displacement	θ (deg.)	–	–
Frequency ratio	f^*	$\frac{f}{f_n}$	–
Strouhal number	St	$\frac{fH}{u_\infty}$	–

dynamics. Some 3D printed rigid nerves of 1 mm thickness were glued along the span of the flap to ensure a two-dimensional adaptation of the proposed devices along the flow direction, as illustrated in Fig. 1(b). The nerves' tips were used as reference points to characterize the flaps' response as they could be easily recognized by means of imaging processing. The tip chord angles (θ_1, θ_2), which were computed from flaps tips in the (x, y) plane, were defined positive in the counterclockwise sense as indicated in the coordinate system shown in Fig. 1.

The Reynolds number was set to vary between $Re = \rho_f u_\infty H/\mu_f \simeq 5 \cdot 10^4$ and $9 \cdot 10^4$, where u_∞, ρ_f and μ_f are respectively the velocity, density, and viscosity of the free-stream. Besides, the coupled dynamics of the fluid–structure interaction problem were characterized by means of the Cauchy number, defined as $Ca = \frac{\rho_f u_\infty^2 H B^3}{2EI}$, where E and I are respectively the Young's Modulus and moment of inertia of the rotation axis, for the calibrated brass foils. Thus, the range of Cauchy number investigated is [16.8, 53.2], which was obtained by varying the wind tunnel velocity, without changing the flaps or the experimental set-up. Moreover, the mass ratio $m^* = \rho_s/\rho_f$ was set to 7000. Additionally, the natural frequency of the system f_n and its structural damping, ξ, were obtained from free-decay tests. The measured natural frequency (13.3 Hz) is very close to the theoretically estimated natural frequency, $f_n = 13.4$ Hz, for an equivalent cantilevered flap. This magnitude can be used to compute the reduced velocity, $U^* = u_\infty/f_n H$, frequently used as the control parameter of fluid–structure interaction problems; however, we will use Ca in the present paper. A summary of the variables and corresponding values characterizing the fluid–structure interaction problem is included in Table 1.

Three different configurations are compared in the present study: (1) the reference baseline case (REF), (2) rigidly mounted flaps, with the same length as the employed flexible flaps (RF), and (3) the described flexible flaps (FF). Note that the REF and RF arrangements are equivalent to the ones included in Camacho-Sánchez et al. (2023); therefore, we will mainly focus the discussion on the flexible flaps case. In order to evaluate the different configurations, we carried out pressure, force, flap deflection, and velocity measurements, which will be described next.

The base pressure distribution on the Ahmed body was obtained through pressure taps distributed in a 3×3 equispaced grid with $\Delta y \simeq 0.26H$ and $\Delta z \simeq 0.19H$, providing with local pressure values $p_i (i = 1, 2, \ldots, 9)$ (see Fig. 1). The measurements were performed

by a 64-channel miniature pressure scanner (with a 4" H_2O range) at a sampling frequency of 200 Hz, providing an accuracy of 0.6 Pa per channel. The pressure was non-dimensionalized using pressure coefficients, defined as

$$c_{p,i} = \frac{p_i - p_\infty}{\rho_f u_\infty^2/2}, \tag{1}$$

where p_∞ represents the free-stream pressure, registered using a Pitot tube placed upstream of the model. The uncertainty associated with $c_{p,i}$ values is below ± 0.001 in the present experiments. In addition, the base drag coefficient (Roshko, 1993) was estimated by means of

$$c_B = -\frac{1}{n}\sum_{i=1}^{n} c_{p,i} \tag{2}$$

where $n = 9$ is the total number of base pressure taps. Furthermore, following previous studies (see e.g. Grandemange et al., 2013b; Lorite-Díez et al., 2020b), the wake asymmetry can be quantified with help of the horizontal and vertical pressure gradients, i.e. g_y and g_z, calculated as

$$g_y = h\frac{\partial c_p}{\partial y} \simeq \frac{1}{2}h\left[\frac{c_{p,6} - c_{p,4}}{y_6 - y_4}\right], \tag{3}$$

$$g_z = h\frac{\partial c_p}{\partial z} \simeq \frac{1}{2}h\left[\frac{c_{p,8} - c_{p,2}}{z_8 - z_2}\right]. \tag{4}$$

Note that this arrangement of nine pressure taps can be considered a relevant and representative set of measurements to accurately estimate base drag and base pressure gradients. This is because the wall pressure distribution in the separated area is, at first order, almost constant in one direction and affine in the other perpendicular direction (direction of the asymmetry) (see e.g. Barros et al., 2017).

The body-axis aerodynamic forces, f_x (drag force) and f_y (side force), were measured using a precise six-axis load cell (with 50N range in x, y directions, with $< 0.5\%$ non-linearity and hysteresis and $< 2\%$ cross-talk effects), connected to the model through four cylindrical supports of diameter 7.5 mm (see Fig. 1). The force balance rotates with the body, sharing the coordinate system. The aerodynamic force coefficients are then obtained as,

$$c_i = \frac{2\ \mathrm{f}_i}{\rho_f u_\infty^2 HW}, \tag{5}$$

where c_i is the force coefficient in the i direction. The force measurements have an associated uncertainty around $\pm$ 0.001 for $c_{x,y}$ coefficients.

Additionally, the flexible flaps deflection and tip deflection angles, θ, were obtained using a high-speed camera (placed at the wind tunnel ceiling, outside the test section) equipped with a 1Mpx CMOS image sensor, with a 1024 × 1024 px resolution up to 6400 fps. The analyzed images were captured at 125 fps, except for the images corresponding to the maximum Reynolds number value, which were taken at 1000 fps, with a 105 mm F/2.8 lens focused on the flap nerves tips to track their motion (an example of the captured images can be seen in Fig. 1b).

To characterize the two-dimensional motion of each flap, a point tracking analysis based on the nerves' tips, was performed. In that regard, the image processing tool named DLTdv8 (Hedrick, 2008), implemented in MATLAB®, was used. The point tracking could be made automatically or guided by the user. In most of our cases, a typical configuration of the tracking parameters was accurate enough to follow the tips of the nerves. However, for the maximum value of the Reynolds (or Ca) number tested here, a deep learning network was needed to track the flaps, whereby all the nerves were tracked during initial and final snapshots to teach the network. The obtained tracking was compared to the original images at several stages during the process to validate the teaching. After that, the coordinates of points were scaled and referenced to the embedding point of the flexible flaps. Subsequently, the flap deflection coordinates could be computed and used to determine the mean deflected position, tip deflection angles or the corresponding spectra from flaps' motion.

Furthermore, the spatial characterization of the near wake was obtained by means of Particle Image Velocimetry (PIV) measurements. The PIV images were captured at a horizontal plane located at $z = 0$ to obtain the velocity fields $\mathbf{u} = (u_x, u_y)$, which will allow us to describe the main features of the recirculating region. The PIV system used a dual pulse laser (2 × 100 mJ/pulse at 532 nm, max. freq: 100 Hz) synchronized through LaVision® PTU-X with an Imager MX 25M (25 Mpx) CMOS camera. The camera was equipped with a 105 mm F/2.8 (we used a F/5.6 aperture in our measurements) optical lens, while the laser sheet was produced using a 1000 mm spherical and a −15 mm cylindrical lenses. A binning operation (×2, ×2) was performed on the camera to obtain a final resolution of 2560 × 2560 px for the acquired images. An initial calibration was conducted using a checkerboard calibrated plate, to properly set the camera focus and the laser plane position and width. This calibration process resulted in a 23.31 px/mm scale and a measurement plane of 222 mm × 222 mm. Additionally, the incoming wind was seeded using an oil-droplet generator, with tracers of diameter $\simeq$ 2 μm. The laser sheet was pulsed with time delays of $dt = 50$ μs, and the set-up acquired 500 pairs of images at 5 Hz, ensuring a sufficient number of images to properly obtain the velocity-averaged fields. After correctly setting the region of interest, velocity vectors were obtained from interrogation windows of 32 × 32 pixels with an overlap of 50%, resulting in a spatial grid of 148 × 98 points, with a resolution below 1% of the body's height. Furthermore, to ensure the repeatability and the accuracy of the results, three different PIV tests were conducted for each experiment, without observing any significant difference between tests. Finally, our measurements have a correlation-based uncertainty (Wieneke, 2015) typically below 3% of the free-stream velocity for both u_x and u_y.

In the following, time-dependent variables will be denoted using lower-case letters a, while time-averaged values will be expressed by means of upper-case letters $A = \overline{a}$. In addition, $\hat{a}$ will denote the instantaneous fluctuating amplitude of the variable a, which will be computed by means of the Hilbert transform, so that $\hat{A}$ will represent the corresponding time-averaged fluctuating amplitude. On the other hand, the notation $| A |$ will be used to indicate the modulus of a variable.

3. Results

3.1. Base flow features

Before describing the effect induced by rear flexible flaps in comparison with the rigid flaps, base flow conditions will be briefly discussed in the present section. In that regard, Fig. 2 includes a summary of the wake features and the aerodynamic loads associated with the baseline configuration in our experimental set-up. As mentioned earlier, the flow around a squareback Ahmed body massively separates at its trailing edges, generating an unsteady, three-dimensional wake with an intense recirculation region near the body as shown in Fig. 2(a1, a2) at $Re \simeq 77000$. The wake topology is depicted by time-averaged flow streamlines alongside contours of time-averaged velocity magnitude, $|U|/u_\infty$. From these wake visualizations, we can obtain the extension and bluffness of the recirculation region, denoted as L_r and H_r, respectively. The recirculation region length, L_r, represents the maximum downstream distance from the body base where $U_x \leq 0$, while H_r denotes the distance between the main recirculating cores within the recirculation region. These cores are identified by red crosses in Fig. 2(a1). At the specified Reynolds number, the recirculation region extends approximately to $L_r/H \simeq 1.42$, with a corresponding width of $H_r/H \simeq 1.02$. This three-dimensional wake is characterized by the destabilization of the Reflectional Symmetry-Breaking (RSB) mode which originates two horizontally-mirrored states of the wake. These deflected states induce random switching in the value of the horizontal base pressure gradient, g_y, between positive, $g_y > 0$, and negative, $g_y < 0$ values, respectively related to P and N wake deflected states (see Fig. 2b1). The behavior of these wake deflected states is described in depth in Grandemange et al. (2013b). These states are highly asymmetric and have an associated averaged horizontal base pressure gradient of $|G_y| \simeq 0.146$ for the baseline case. This dynamics can be represented by the Probability Density Function (PDF) of g_y, as it can be seen in Fig. 2(c1), that depicts the probability of exploring P and N states by the wake. On the other hand, the wake remains vertically fixed but exhibits a slight deflection. This minor vertical asymmetry arises from the ground's presence, resulting into a small vertical pressure gradient, g_z, characterized by a single peak in the corresponding PDF (see Fig. 2a2, b2 and c2, respectively).

In addition, cross-wind conditions are also studied in the present study. Therefore, the near wake topology observed at $\beta = 5, 10°$ for the baseline case is respectively depicted in Fig. 2(d1, d2) at the horizontal plane placed at $z = 0$ for $Re \simeq 77000$. As shown therein, the near wake becomes asymmetric, inducing a mean horizontal base pressure gradient of $G_y = 0.141$ and 0.136 at $\beta = 5, 10°$, respectively. It is remarkable how the $|G_y|$ is almost constant at aligned and cross-wind conditions, due to the presence of the RSB mode.

Finally, the evolution of the base drag, C_B, and the drag coefficients, C_x, with Re is depicted in Fig. 2(e) for the three tested flow orientations. The base pressure does not change with the Reynolds number, however, the drag is reduced as Re increases. As we have performed the experiments at moderate Reynolds, $Re \in (48000, 87000)$, the friction drag still has some importance, and therefore, C_x is reduced when the wind velocity increases. At yaw, both C_x and C_B increase with β, which may be associated with the appearance of streamwise vortices developing at the model longitudinal edges (McArthur et al., 2018).

3.2. Effect of flexible flaps on the drag coefficient

The aerodynamic effect of the rear passive devices, i.e. rigid and flexible flaps, on the body-axis (local) drag coefficient and base pressure is next analyzed with help of Fig. 3. In order to isolate the effect of the flaps, both drag, C_x, and base drag, C_B, coefficients have been made relative to the reference case as $\Delta C_i^j = C_i^j - C_i^{REF}$ where j is the flap type (RF, FF) and i the aerodynamic coefficient at the given Re or β conditions.

The rigid flaps are able to slightly reduce the drag coefficient under aligned conditions (see Fig. 3a), by recovering base pressure, as it is depicted in Fig. 3(b). Although the reduction of C_B is much larger, the additional length of the flaps presumably increase the total friction drag of the body, enhancing C_x. Under yawed conditions, the rigid flaps do neither recover base pressure nor reduce drag, but on the contrary, increase both coefficients. This is possibly linked to the additional friction drag and their interaction with the streamwise rotating vortices that appear under crosswind configurations. The same features were observed in Camacho-Sánchez et al. (2023) for a similar set-up in the same wind tunnel.

Concerning the flexible flaps, they are shown to efficiently reduce drag reduction and retrieve the base pressure, as depicted in Fig. 3, which is particularly evident at low values of Ca. Notably, the relative reduction in ΔC_B exceeds that of ΔC_x, highlighting the additional friction drag introduced by the flaps. However, this difference in relative changes is less pronounced compared to the RF configuration, attributed to the self-adaptive nature of flexible flaps. Moreover, under crossflow conditions, the FF configuration effectively recovers base pressure for low Ca values, with an increasing ΔC_B observed with yaw angle. For the drag, the trends become more intricate for low Ca values, although the FF remain more efficient than the RF configuration. The base pressure recovery and drag reduction values obtained for flexible flaps exhibit a similar behavior to that of hinged-like flaps showed in Camacho-Sánchez et al. (2023), as they represent equivalent systems within small flexibility ranges. However, we observe a significant increase in ΔC_x and ΔC_B for large Ca values, corresponding to the highest flexibility of the flaps. The critical Ca value

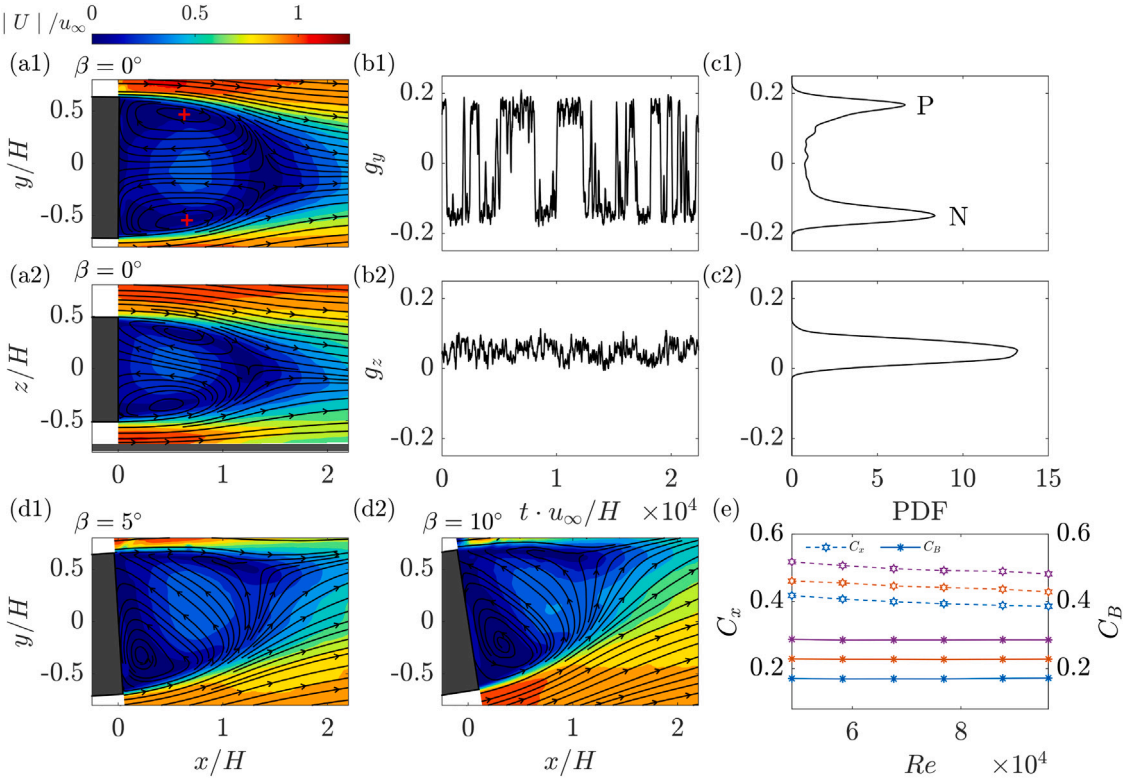

Fig. 2. Flow topology at $Re \simeq 77000$ for the baseline case. Time-averaged velocity magnitude contours and flow streamlines on the horizontal ($z = 0$) plane at (a1) $\beta = 0°$, (d1) $\beta = 5°$, and (d2) $\beta = 10°$, and the vertical ($y = 0$) plane for the reference case at $\beta = 0°$ (a2). Vortex recirculation cores in the horizontal plane are highlighted in (a1) by red crosses. (b1, b2) Respective temporal evolution of horizontal (g_y) and vertical (g_z) base pressure gradients (defined in Eqs. (3) and (4)). (c1, c2) Probability Density Functions (PDF) of horizontal (g_y) and vertical (g_z) base pressure gradients, respectively. Note that PDF (g_y) presents two wake states P and N, respectively associated with $g_y > 0$ and $g_y < 0$ wake states. (e) Evolution of drag, C_x (empty symbols, dashed lines), and base drag, C_B (filled symbols, solid lines) with Re for different yaw angles ($\beta = 0°$: blue, $\beta = 5°$: orange, $\beta = 10°$: purple). (For interpretation of the references to color in this figure legend, the reader is referred to the web version of this article.)

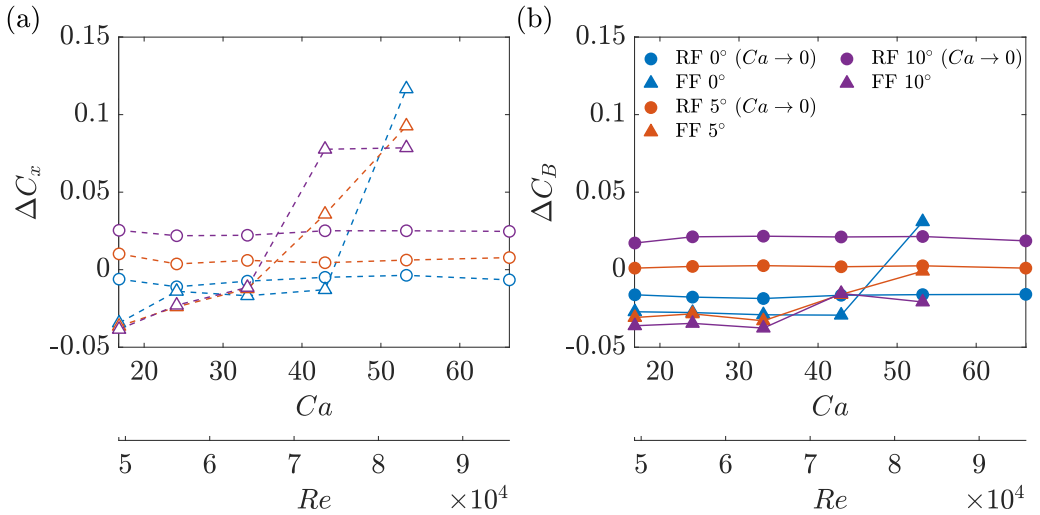

Fig. 3. Evolution of the relative (a) drag (empty symbols and dashed lines) and (b) base drag (filled symbols and solid lines) coefficients with Ca (or Re) for rigid (RF, circles) and flexible (FF, triangles) flaps configurations with respect to the baseline case under the different tested yaw angles ($\beta = 0°$, blue; $\beta = 5°$, orange and $\beta = 10°$, purple). (For interpretation of the references to color in this figure legend, the reader is referred to the web version of this article.)

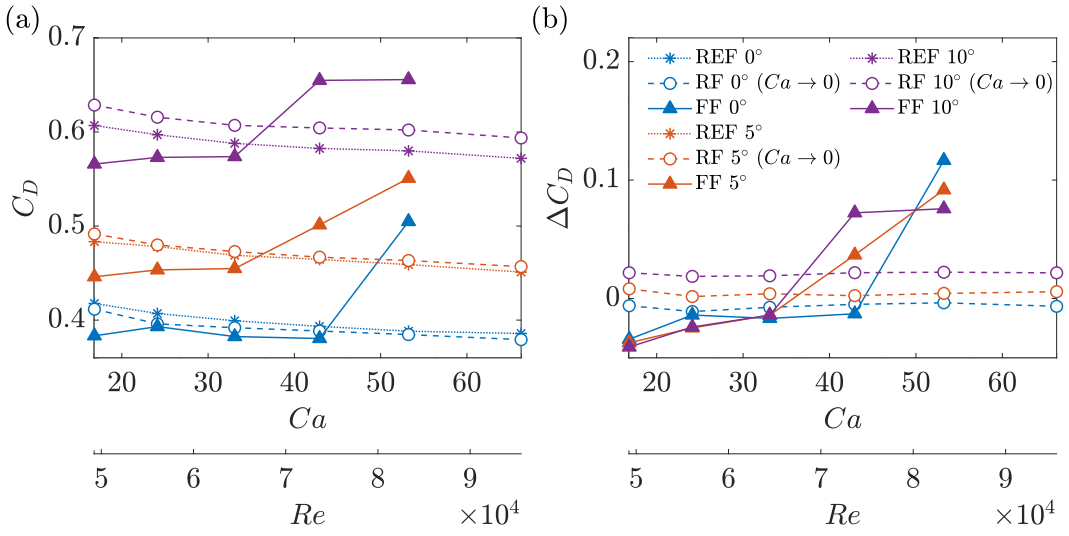

Fig. 4. Evolution of the (a) global drag coefficient, C_D, and (b) its relative variation, ΔC_D, with Ca (or Re) for the baseline case (REF, asterisks and dotted lines), rigid flaps (RF, circles and dashed lines) and flexible flaps (FF, triangles and solid lines) for the different tested yaw angles ($\beta = 0°$: blue, $\beta = 5°$: orange and $\beta = 10°$: purple). (For interpretation of the references to color in this figure legend, the reader is referred to the web version of this article.)

defining this increase and its magnitude vary with the yaw angle. Finally, there appears to be a saturation point in the increase of ΔC_x and ΔC_B for $\beta = 10°$.

We will next analyze the impact of the tested passive solutions on the global drag force (referred to the incoming flow direction), denoted as C_D. Since the force balance co-rotates with the model, this coefficient can be computed using the following force composition (Hucho and Sovran, 1993): $C_D = C_x \cos(\beta) - C_y \sin(\beta)$. In this context, Fig. 4 illustrates the evolution of both the absolute (C_D) and relative global drag coefficient (ΔC_D) with Ca for the tested configurations. For the baseline case, as the velocity increases, the C_D decreases, on account of the friction drag reduction with Re. Under crosswind conditions, C_y deviates from 0, thus contributing to increase C_D, as depicted in Fig. 4(a) for the reference case.

Mounting rigid flaps results in a marginal reduction in global drag, C_D, at $\beta = 0°$. Again, the additional body length introduced by the flaps increases friction drag and the lateral force, C_y, rendering these flaps counterproductive for drag reduction under cross-flow (see Fig. 4b), in line with the findings of Lorite-Díez et al. (2020a).

Conversely, the flexible flaps (FF) configuration notably improve the performance of rigid flaps in terms of reducing C_D at low Ca values (see Fig. 4a, b). Regarding the relative drag change with respect to the reference case, ΔC_D, the reduction remains almost constant for any orientation between the model and the incoming wind. Thus, it seems that the self-adaptation of the flaps to the incoming wind compensates for the drag increase induced by the additional body length associated with the lateral flaps. However, at higher values of Ca, i.e. as the flap flexibility increases, the drag trend changes significantly, as it has been observed for C_x and C_B. This drag increase depends on β and may be associated with the appearance of a new deformation mode of the flaps. A detailed analysis of the response of the flexible flaps' response follows below.

3.3. Flaps deformation

The averaged deformation angles of the flaps' tips, denoted as $\Theta_{1,2}$, are illustrated in Fig. 5(a) for all the tested flow conditions. Under aligned flow conditions, both flexible flaps deform symmetrically. For $Ca < 45$, the tip deflection remains nearly constant, being 4° approximately. However, as Ca increases, there is a sharp jump in the mean deformation, reaching up to 19°, coinciding with the abrupt increase in drag or base drag coefficients reported earlier. Under yawed conditions, for $Ca < 40$, the maximum averaged deformation observed for $\beta = 5°$ and 10° is 6° and 7°, respectively. At these low Ca numbers, the mean deformation angle of the leeward flap (Θ_1) increases with β, while that of the windward flap (Θ_2) remains relatively constant at $\beta = 0°$ and 5°, with only a slight increase observed at $\beta = 10°$.

At higher numbers of Ca and under yawed conditions, the asymmetry in the flap deformation is evident. At $\beta = 5°$, the leeward flap (Θ_1) maintains a similar deformation angle observed for the low Ca range, while the deformation angle of the windward flap (Θ_2) increases. For the maximum tested value of Ca, the deformation angle increases for both flaps, reaching approximately the same value of $\simeq 19°$. At $\beta = 10°$, both windward and leeward flaps exhibit similar deformation trends for $Ca > 45$, with deformation angles that increase significantly and then saturate close to $\simeq 21°$ at the maximum tested value of Ca. Interestingly, the yaw angle does not play a significant role in the maximum averaged deformation angles, Θ, reached by the two flaps at $Ca \simeq 53$.

Let us now analyze the amplitude of the flaps angular oscillations with the help of Fig. 5(b). Under aligned conditions, it is observed that the flexible flaps deform with very low-amplitude oscillations for $Ca < 45$, remaining below $\hat{\Theta} \leq 1°$ (see Fig. 5b).

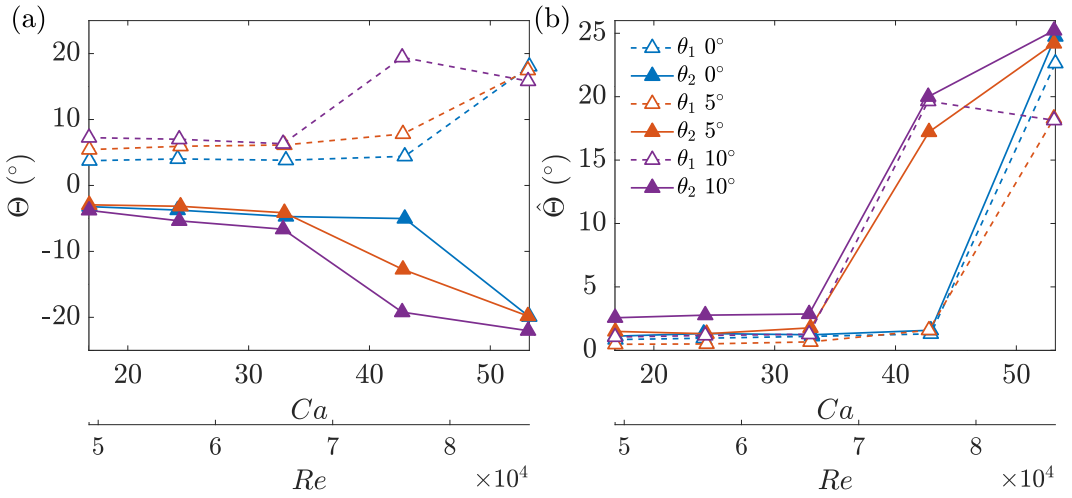

Fig. 5. Evolution of (a) the averaged flap deflection angle, Θ, and (b) the mean fluctuating amplitude, $\hat{\Theta}$, of flap deformation angle with respect to Ca (or Re) for the different yaw angles ($\beta = 0°$: blue, $\beta = 5°$: orange and $\beta = 10°$: purple). (For interpretation of the references to color in this figure legend, the reader is referred to the web version of this article.)

Conversely, around $Ca \simeq 53$, both flaps start to oscillate with larger amplitudes, $\hat{\Theta} \simeq 23°$, which closely resembles the mean deformation angle, $\Theta \simeq 19°$. This indicates a change in the deformation mode for both flaps. To provide a clearer visualization of the flaps' deformation, supplementary materials 1 and 2 include two videos where the flaps motion at respectively $Ca \simeq 43$ and $Ca \simeq 53$, is depicted for the two described behaviors.

Under crosswind conditions, the oscillations of the flaps exhibit an asymmetric behavior similar to the averaged tip deflection angle, Θ (see Fig. 5b). Initially, at small Ca values, the flaps undergo low-amplitude oscillations. However, there is a sudden increase in the amplitude of the oscillations at larger Ca values. At $\beta = 5°$, these enhanced fluctuations appear asymmetrically, with the windward flap (θ_2) depicting strong oscillations at lower Ca values (similar to the trend observed for the mean deformation angle in Fig. 5a). Conversely, at $\beta = 10°$, both the leeward and the windward flaps start to oscillate for the same Ca value, reaching a saturated state around $Ca \simeq 53$. Similar to the mean flaps deformation angle, Θ, the amplitude of oscillations increases up to a global constant level, of approximately $\hat{\Theta} \simeq 25°$, irrespective of β angle. However, the leeward flap (θ_1) reaches weaker oscillations under yawed conditions for the whole range of Ca, which may be associated with the flow asymmetry illustrated in Fig. 2 (d1, d2). After describing the mean deflection and the averaged oscillations of the flaps, we will next analyze the unsteady motion of the flaps and their deformed shape. In Fig. 6, we present the averaged deformation of the entire flap (illustrated by the pink solid lines with asterisks) alongside the corresponding contours of the probability density function (PDF) for each instantaneous positions of both flaps. The averaged flap deformation is represented in both deformation directions, x and y. The PDFs are normalized to give a unity value upon integration of the distribution; however, for the sake of clarity of representation, a limit of 0.1 has been set up for the colormap.

At aligned conditions, both flaps exhibit a symmetric behavior, as shown in Fig. 5. Consequently, only the θ_2 flap is depicted in Fig. 6(a, b). In line with the behavior described for $Ca < 45$, the flexible flaps deform inwardly with a mild mean deflection and very small-amplitude oscillations (see Fig. 6a). Conversely, at $Ca \simeq 53$, the averaged deformation is significantly larger, accompanied by a wider extension of oscillations around it (see Fig. 6b).

On the other hand, the asymmetric behavior of the flaps under $\beta = 5°$ is evident in Fig. 6(c–f). For low values of Ca (see Fig. 6c, e), the windward flap (θ_2) depicts a stronger averaged deformation than the leeward flap (θ_1). In addition, the associated PDFs display a higher level of oscillations for the windward flap, as it was observed in Fig. 5. At $Ca \simeq 53$ (see Fig. 6d, f), both flaps deflect in a nearly symmetric way, with equivalent mean deformation and similar probabilities of deformations, displaying a strong oscillating pattern (see Fig. 6e, f).

To deeper analyze the temporal behavior of the flaps deformation, we depict in Fig. 7(a1–b2) the temporal evolution of the fluctuating tip deformation angle, $\hat{\theta}$, and the associated Power Spectral Density (PSD) spectra under aligned conditions for $Ca \simeq 43$ and $Ca \simeq 53$, respectively. At low Ca values, both flaps tips exhibit in-phase movement, depicting very subtle high-frequency, low-amplitude oscillations alongside with occasional switches between relatively large positive and negative values of $\hat{\theta}$. This behavior resembles the dynamics observed for three-dimensional wakes when the RSB mode is present, as evidenced by the time evolution of g_y shown in Fig. 2(b1). Interestingly, the flexible flaps seem to respond to the RSB mode acting in our experiment, indicating a fluid–structure interaction mechanism similar to that reported in Camacho-Sánchez et al. (2023). Such low-amplitude oscillations, superimposed on the random switching, are well identified in the spectrum of $\hat{\theta}$ (see Fig. 7b1), where a peak at $f^* \simeq 2$ emerges. This value corresponds to $St \simeq 0.11$, which is close to the shedding frequency values reported for this type of flows (Lorite-Díez et al., 2020b).

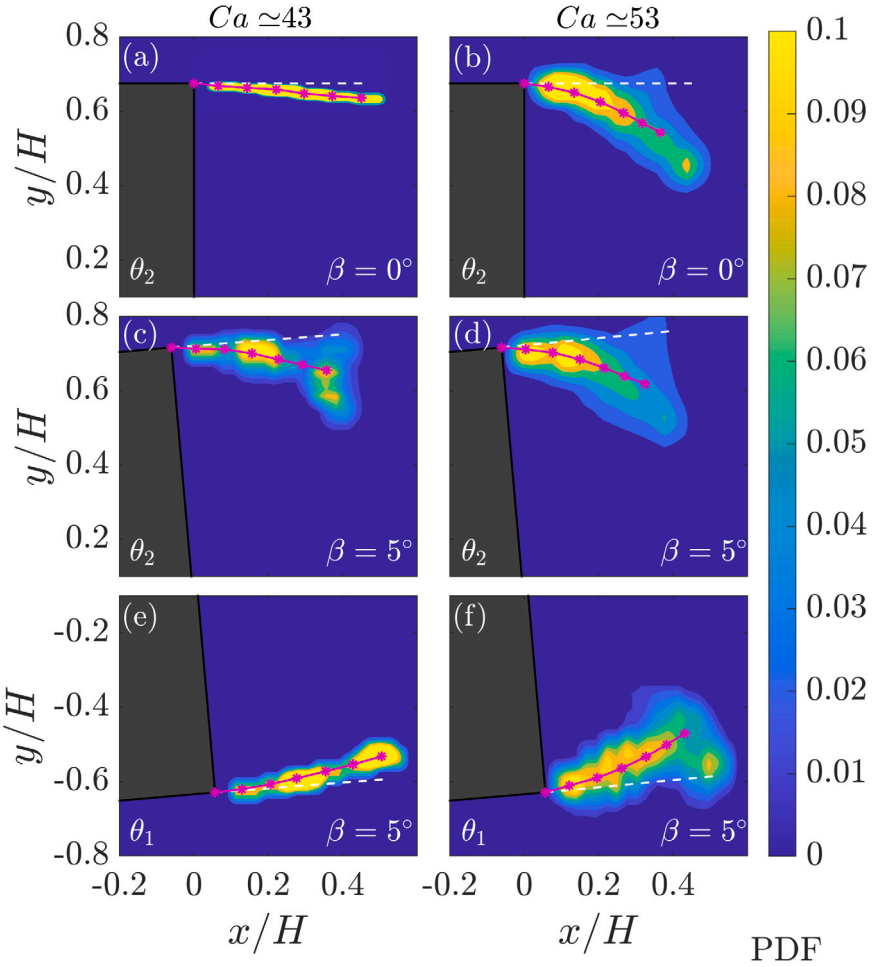

Fig. 6. Averaged flap deformation shape (illustrated by the pink solid lines with asterisks) alongside the contours of the probability density function (PDF) of the instantaneous flap deformations. Figures (a, b) correspond to aligned conditions while figures (c, d, e, f) represent $\beta = 5°$ flow conditions for both low, $Ca \simeq 43$, and large, $Ca \simeq 53$, values. A white dashed line is included to indicate the position of a rigid flap for reference purposes.

We have used this temporal dynamics to conduct a modal decomposition analysis of the flap deformation, following the procedure outlined in García-Baena et al. (2021a), aiming to identify the dominant deformation modes and compare them with those characterizing the free deformation of cantilevered beams. In that regard, we have first selected the most energetic deformation modes in the corresponding Power Spectral Density (PSD) spectra. Then, the original signal is band-pass filtered around the dominant identified peaks. After that, the shapes (y_i) of the first ($i = 1$) and second ($i = 2$) Euler–Bernoulli free modes of deformation for a cantilever beam are computed following (Rao, 2011):

$$y_i = y_i^f\,[\sin\beta_i x - \sinh\beta_i x - \alpha_i(\cos\beta_1 x - \cosh\beta_1 x)], \tag{6}$$

where (x_i^f, y_i^f) is the band-pass filtered deformation of the flaps in the mode i, with $\alpha_i = (\sin\beta_i B + \sinh\beta_i B)/(\cos\beta_i B + \cosh\beta_i B)$, $\beta_1 B = 1.875$ and $\beta_2 B = 4.694$.

This procedure has been applied to the deformation illustrated in Fig. 7(a1, b1). For low Ca values, there is only a deformation mode so the band-pass filtering is not needed. The corresponding first Euler–Bernoulli deformation mode (x_1, y_1), represented by pink solid lines, is compared to the actual location of the flexible flap (x^f, y^f), depicted with blue dashed lines with circles, at two extreme locations of the flaps in Fig. 7(c1). At first sight, a clear resemblance is observed, meaning that the deformation of the plates can be properly characterized by the first Euler–Bernoulli deformation mode. Moreover, it is seen that the flap deforms with a very low spatial amplitude at this Ca value. Finally, the energy associated to the identified first deformation mode is illustrated in Fig. 8 for both flaps and different values of β.

For $Ca \simeq 53$, the dynamics of flaps considerably changes. Notably, the temporal evolution of flap tip oscillation $\hat{\theta}$ has a different behavior. Instead of exhibiting random switching dynamics as seen in Fig. 7(a2), it displays a quasi-periodic behavior, seemingly composed of two main frequencies. This temporal evolution is characterized by a phase difference between the deformations of both

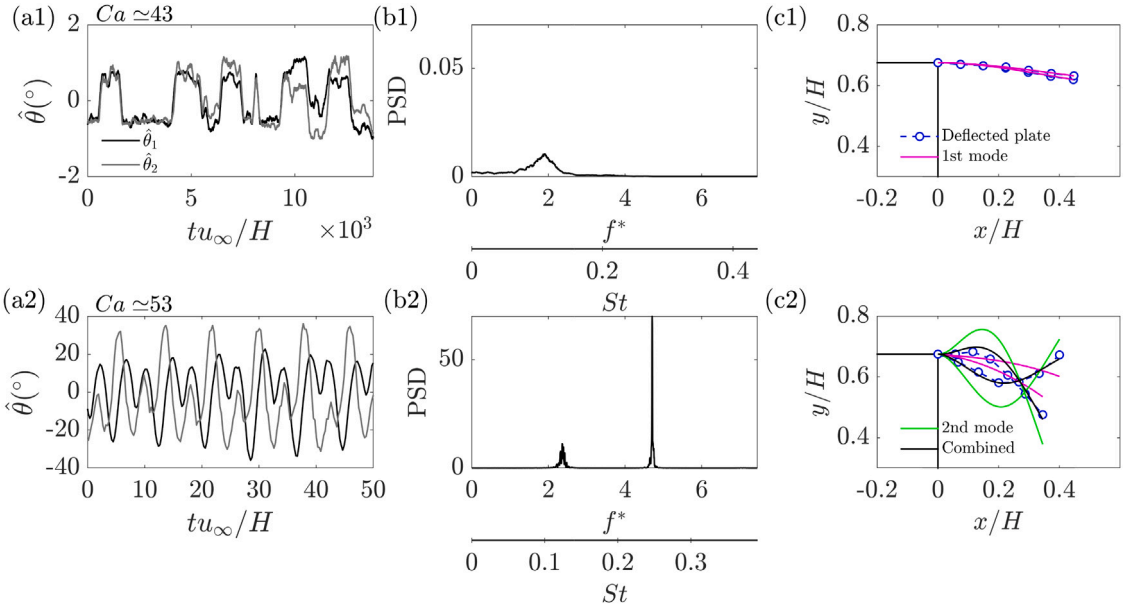

Fig. 7. (a1, a2) Temporal evolution of fluctuating flap deflection angles ($\hat{\theta}_1$: black, $\hat{\theta}_2$: gray) at respectively $Ca \simeq 43$ and $Ca \simeq 53$ under aligned conditions. (b1, b2) Corresponding Power Spectral Density (PSD) distribution for the fluctuating flap deflection angles (just $\hat{\theta}_1$) displayed in (a1, a2). (c1, c2) Instantaneous extreme flap deflections: actual flap position (blue circles with dashed lines), flap deflection corresponding to the identified first deformation mode (pink solid lines), the identified second deformation mode (green solid lines) and their combination (black solid lines). (For interpretation of the references to color in this figure legend, the reader is referred to the web version of this article.)

flaps, $\hat{\theta}_1$ and $\hat{\theta}_2$. Supplementary Material 2 provides a clear visualization of this behavior. As shown in Figs. 5 and 6, the oscillation amplitudes are significantly larger compared to lower Cauchy numbers. The corresponding Power Spectral Density (PSD) spectrum reveals two distinct frequency peaks. The first peak, similar to that observed at low values of Ca, can be seen in Fig. 7(b2). However, the associated frequency values f^* and St are slightly larger than before due to an acceleration of the coupled dynamics, a common feature in more flexible fluid–structure systems. Moreover, a dominant frequency component emerges in a second peak at $f^* \simeq 4.7$ and $St \simeq 0.25$, which is close to be the second harmonic of the previous low-frequency peak.

Here, to apply the modal decomposition, we need to band-pass filter the flaps deformation signals to obtain the deformation corresponding to the first (x_1^f, y_1^f, $f^* \simeq 2.3$) and the second (x_2^f, y_2^f, $f^* \simeq 4.7$) frequency peaks. Then, the shapes of the first (x_1, y_1) and second (x_2, y_2) Euler–Bernoulli deformation modes are obtained from Eq. (7) using the filtered deformation signals. The first Euler–Bernoulli deformation mode (x_1, y_1) is depicted in pink solid lines while the second deformation mode (x_2, y_2) is shown in green solid lines (see Fig. 7c2). Additionally, the combined deformation of both modes is obtained as

$$y_t = \frac{E_1}{E_T} y_1 + \frac{E_2}{E_T} y_2 \tag{7}$$

where y_t is the total combined deformation of the flap. E_1 and E_2 are the energy associated to the band-pass filtered signals for the first and second frequency peaks. Note that the energy is computed by the integration of the density spectra around each frequency peak. E_T is the total energy of deformation of the flap. The combined deformation from the first and second Euler–Bernoulli modes, y_t, depicted in black solid lines, is compared with the actual flap deformation (x^f, y^f) at two extreme positions (blue dashed lines with circles) in Fig. 7(c2). Despite the large deformations and the complex load on the plates produced by the incoming flow and the near wake, the combination of the first and second free deformation modes of a cantilevered beam effectively captures the flaps behavior.

The energy associated to each mode, E_1, E_2, is depicted against Ca in Fig. 8 for both flaps. That said, under aligned conditions and $Ca < 45$, the energy corresponding to the first mode is almost constant and similar for both flaps, with no trace of the second mode (see Fig. 8a). However, for the maximum tested value of $Ca \simeq 53$, there is a sharp increase of the energy associated to both first and second modes (as it could be also seen in Fig. 7b2).

When the model is not aligned with the flow, at a yaw angle of $\beta = 5°$, for low values of Ca, the first mode is more intense in the windward flap (θ_2) than in the leeward flap (θ_1), reflecting the asymmetric response of the flaps under crosswind conditions (see Fig. 8b). Then, around $Ca \simeq 43$, the windward flap (θ_2) starts to oscillate with large amplitude following the second mode while the leeward flap (θ_1) remains oscillating mainly in the first mode. At the maximum tested value of Ca, both flaps oscillate with a similar amplitude in the second mode. A similar response from the leeward (θ_1) and windward (θ_2) flaps is obtained at $\beta = 10°$, for low values of Ca, as it can be seen in Fig. 8(c). At this yaw angle, the energy associated to the second mode grows at the same Ca value for both flaps and then saturates at the maximum tested value of Ca. Interestingly, the total energy of both modes is

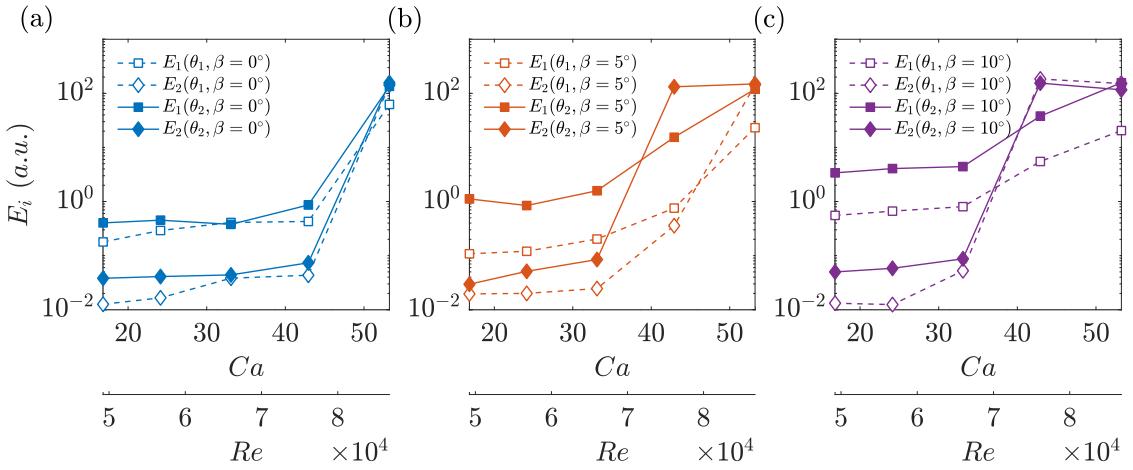

Fig. 8. Evolution of the corresponding energy for the first (squares) and second (diamonds) deformation modes, E_1 and E_2, with Ca (or Re). Energy associated to each flap (θ_1: dashed lines, θ_2: solid lines) at the different tested yaw angles (a) $\beta = 0°$: blue (b) $\beta = 5°$: orange and (c) $\beta = 10°$: purple). (For interpretation of the references to color in this figure legend, the reader is referred to the web version of this article.)

almost the same at $Ca \simeq 53$ for all the tested flow orientations, as it was already seen in Fig. 5(b), indicating a possible limit in the energy transfer between the flexible flaps and the wake dynamics. The growth in energy of the second deformation mode at high Ca values is seen to increase the mean angular deformation of the flaps and their associated fluctuating amplitude, being this behavior detrimental for aerodynamic purposes, as it increases C_x and C_B. The role of both deformation modes on the near wake dynamics and their implications in drag changes will be described in the next section.

3.4. Wake dynamics and fluid–structure interaction mechanism

We will next analyze the coupling between flaps deformation and wake features based on near wake visualizations, pressure measurements and deformation oscillations. The analysis is restricted to $\beta = 0°$, however, the interpretation of the fluid–structure interaction mechanism remain applicable under yawed conditions.

At low Ca values, the temporal evolution of fluctuating flap deflection angles, $\hat{\theta}_{1,2}$, shown in Fig. 7(a1), closely mirrors the dynamics of the horizontal base pressure gradient, g_y, depicted in Fig. 2(b1). This close resemblance suggests a strong link between the Reflectional-Symmetry-Breaking (RSB) mode and the induced flaps deformation. In order to analyze this coupling, Fig. 9(a) displays the normalized contours of the PDFs corresponding to the horizontal base pressure gradient, g_y, at the tested Re for the baseline case. This type of representation is a conventional way to characterize the dynamics of the RSB mode, as it can be seen in Evrard et al. (2016), Barros et al. (2017), Lorite-Díez et al. (2020b) and Camacho-Sánchez et al. (2023). The PDFs are normalized with the corresponding maximum value of each PDF. As discussed in Section 3.1, the RSB mode displays a random switching between equivalent deflected near wake states, P and N, which respectively correspond to positive ($g_y > 0$) and negative ($g_y < 0$) values of horizontal base pressure gradient. Under aligned conditions, both wake states nearly feature the same probability (see Fig. 9a). This equal probability to explore P and N states is maintained during the tested range of Re for the baseline case. As shown by Camacho-Sánchez et al. (2023), rigid flaps are able to turn the near wake symmetric, removing the influence of RSB mode on the base pressure distribution, which makes the g_y to be 0 at aligned conditions. The same behavior is reported here and the corresponding results are omitted for the sake of conciseness.

When the flexible flaps are implemented, both branches of the horizontal base pressure gradient PDF (g_y), corresponding to the P and N states, are preserved for $Ca < 45$ (see Fig. 9b). However, the magnitude of the horizontal base pressure gradients associated with these deflected states, $|G_y| \simeq 0.095$, is much smaller than that of the reference case ($|G_y| \simeq 0.141$). At $Ca \simeq 53$, the PDF exhibits a centered distribution of g_y, suggesting a symmetric base pressure distribution in average. These wake changes are attributed to the appearance of the second deformation mode identified in Section 3.3. The strong flap deformations and the corresponding high amplitude oscillations observed for both flexible flaps at $\beta = 0$ reduce the averaged wake asymmetry, suppressing any wake deflected state (see Fig. 9b).

For the bi-stable range of Ca, i.e. $Ca < 45$, a proposed mechanism for the fluid–structure interaction between flexible flaps and RSB mode is sketched in Fig. 9(c). In a P wake deflected state ($g_y > 0$), the positive base pressure gradient may induce an inward deformation of the θ_1 flap, resulting in positive values of $\hat{\theta}_1$, while simultaneously inducing an outward deformation of the other flap, also yielding positive $\hat{\theta}_2$ values. Conversely, a N wake deflected state ($g_y < 0$) exhibits opposite yet equivalent behavior. Therefore, there is an in-phase relationship between the temporal signal of g_y and the time evolution of $\hat{\theta}_{1,2}$, similar to the one reported in Camacho-Sánchez et al. (2023). However, in the current configuration, as the associated Ca for the flexible flaps is larger, the interaction with RSB mode starts at lower Re value. On the other hand, when $Ca > 45$, the appearance of the second mode of deformation removes the presence of RSB modes from the near wake, altering the flaps response. This overall behavior is

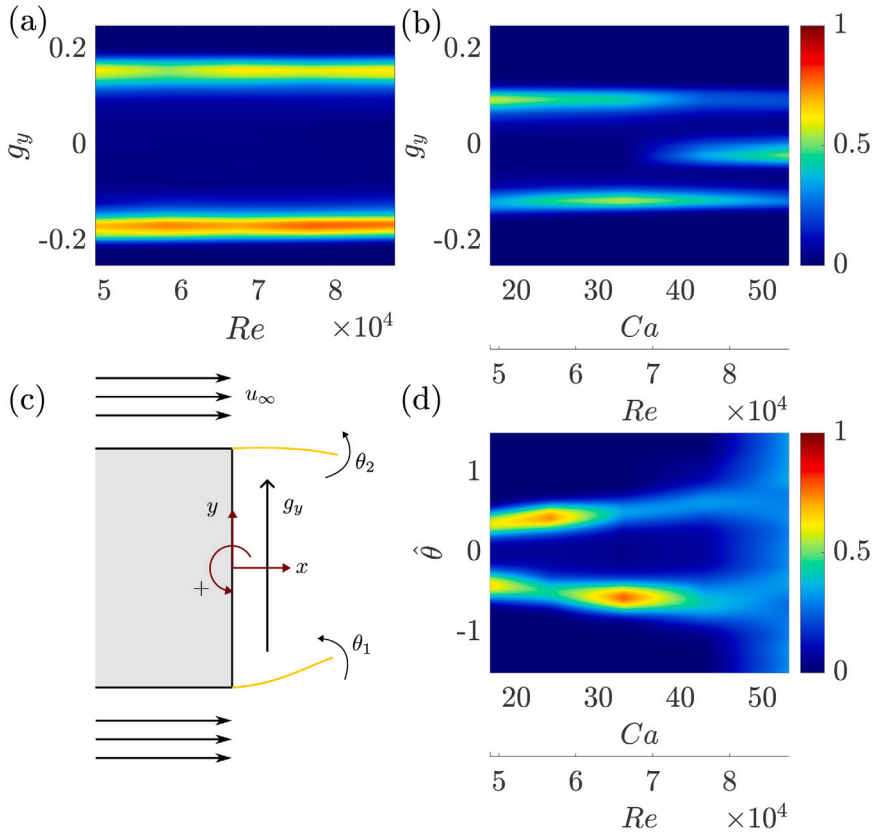

Fig. 9. (a, b) Contours of horizontal base pressure gradient PDFs from g_y at the tested Reynolds numbers Re (and Ca), for the (a) REF and (b) FF configurations. (c) Sketch of the interaction between the flaps deflection and the RSB mode (under P state, $g_y > 0$). (d) PDF of the observed deflected angle at the tested Reynolds numbers Re (and Ca) for FF configuration. The PDFs are normalized with their corresponding maximum value.

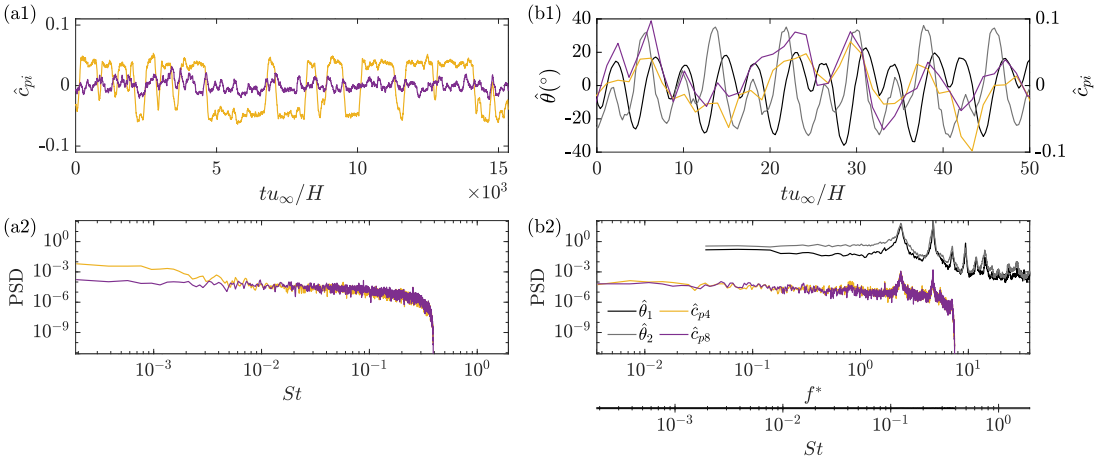

Fig. 10. (a1) Temporal evolution of the fluctuating pressure coefficients, $\hat{c}_{pi}$ (Pressure tap 4, $\hat{c}_{p4}$, in purple and pressure tap 8, $\hat{c}_{p8}$, in yellow) for the baseline case at $Re \simeq 87000$ under aligned conditions. (b1) Temporal evolution of the fluctuating flap deflection angles ($\hat{\theta}_1$: blue, $\hat{\theta}_2$: orange) alongside the fluctuating pressure coefficients, $\hat{c}_p$ (Pressure tap 4, $\hat{c}_{p4}$, in purple and pressure tap 8, $\hat{c}_{p8}$, in yellow), at $Ca \simeq 53$ under aligned conditions. (a2, b2) Corresponding Power Spectral Density (PSD) distribution for the fluctuating pressure coefficients and flap deflection angles depicted in (a1, b1). (For interpretation of the references to color in this figure legend, the reader is referred to the web version of this article.)

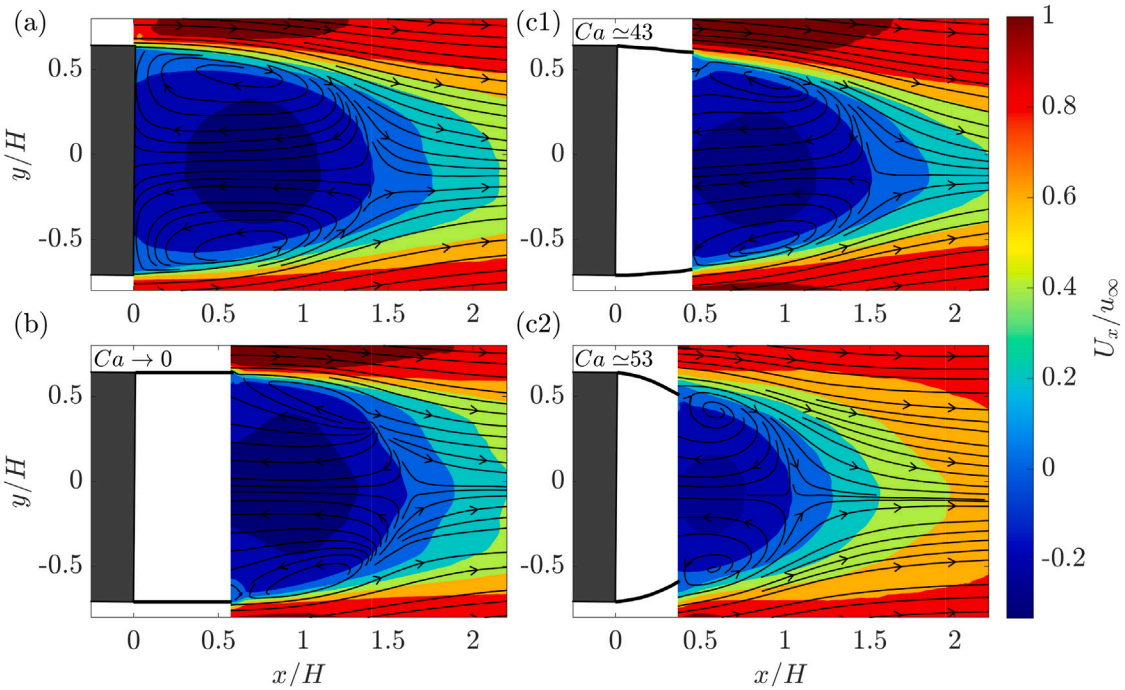

Fig. 11. Time-averaged flow at the horizontal plane placed at $z = 0$ for: (a) baseline case, (b) rigid flaps at $Re \simeq 77000$ and (c1, c2) flexible flaps at $Ca \simeq 43$ ($Re \simeq 77000$) and $Ca \simeq 53$ ($Re \simeq 87000$), respectively. The time-averaged flow is illustrated with contours of averaged streamwise velocity (U_x) alongside averaged flow streamlines (U_x, U_y).

illustrated in Fig. 9(d), which presents the normalized contours of combined PDFs of $\hat{\theta}$ against Ca (and Re). There, it is observed that for $Ca < 45$, the flaps exhibit a bi-stable behavior, exploring positive and negative relative orientations, $\hat{\theta}_i$, with nearly the same probability. Conversely, with the emergence of the second mode of deformation ($Ca > 45$), the flaps explore a broader range of tip angular deformations, resulting in a nearly uniform and symmetric PDF.

Let us next analyze the temporal interaction between the flexible flaps and the wake in this second deformation mode. We will start describing the wake unsteadiness for the baseline case at $Re \simeq 87000$. Fig. 10(a1) presents the temporal evolution of the pressure coefficient fluctuations ($\hat{c}_p$) at the pressure taps 4 (located on the base left side) and 8 (located on the base upper side). The random switching of pressure levels at tap 4 evidences the presence of RSB mode in the horizontal direction, while the wake position remains vertically fixed (tap 8). The associated Power Spectral Density (PSD) spectra are illustrated in Fig. 10(a2). The slow yet large-amplitude switches between the P and N wake deflected states are represented by the large energy at low frequency ranges of the pressure coefficient associated with the pressure tap 4 (see Fig. 10a2). Furthermore, both base pressure measurements exhibit subtle frequency peaks with lower amplitude at higher frequencies, possibly corresponding to vortex shedding or bubble pumping, however, their significance is affected by the temporal filtering induced by the pressure tubing.

For the flexible flaps, we represent together the temporal evolution of the fluctuations of their deformation angles, $\hat{\theta}_1$ and $\hat{\theta}_2$, and the temporal evolution of the pressure coefficient fluctuations ($\hat{c}_p$) at the same locations as before (taps 4 and 8). At $Ca \simeq 53$ ($Re \simeq 87000$), we can see that coupled dynamics are governed by the emergence of the second deformation mode (see Fig. 10b1). This flap behavior is seen to remove the RSB mode from the wake, suppressing the bistable behavior of the base pressure measurements or the deformation of the flaps. However, it causes a forcing on the near wake, evidenced by the appearance of two pronounced frequency peaks in the spectra corresponding to the fluctuating pressure coefficients of tap 4 and 8 (see Fig. 10b2). The differences in the range of resolved frequencies in the spectra are attributed to the distinct acquisition frequencies and the different temporal duration of our measurements. These new frequency peaks illustrate the temporal synchronization between the deformation modes of the flaps and the wake unsteadiness.

In addition, we next investigate the relationship between flaps response and near wake flow topology. In that regard, the time-averaged velocity fields in the horizontal plane, $z = 0$, are depicted in Fig. 11 at $\beta = 0°$. To illustrate the characteristics of the recirculation region, contours of time-averaged streamwise velocity (U_x) are depicted alongside time-averaged flow streamlines (U_x and U_y). Fig. 11(a, b and c1) compares the near wake features of the baseline, rigid flaps and flexible flaps cases for $Re \simeq 77000$ ($Ca \simeq 43$). Moreover, the near wake corresponding to the flexible flaps for $Ca \simeq 53$ is included in Fig. 11(c2). In the baseline case, the near wake is statistically symmetric, although asymmetric P and N deflected wake states are present in the recirculation region. Thus, an horizontal symmetrical distribution of the flow is associated with a symmetrical PDF of the horizontal base pressure gradient (g_y). When the rigid flaps are installed (see Fig. 11b), the recirculation region becomes longer than that of the reference

case ($L_r/H \simeq 1.61$) since the presence of the flaps physically separates the recirculation region cores from the body base, causing base pressure recovery observed in Fig. 3(b). The pressure recovery achieved by the rigid flaps is also linked to the suppression of the RSB mode under this configuration (Bonnavion and Cadot, 2018).

For $Ca \simeq 43$, the flexible flaps also increase the length of the recirculation region ($L_r/H \simeq 1.51$) and decrease their bluffness ($H_r/H \simeq 0.97$), compared with the reference case (see Fig. 11c1). These alterations in the topology of the recirculation region may account for the achieved base pressure recovery and the subsequent drag reduction illustrated in Fig. 3. As the relative flexibility increases to $Ca \simeq 53$, Fig. 11(c2) shows a more pronounced mean deformation, significantly reducing the size of the recirculation region ($L_r/H \simeq 1.04$, $H_r/H \simeq 0.93$). This diminished recirculation region exhibits two strong recirculating cores, leading to an important decrease in the base pressure level. In addition, the significant oscillations of the flexible flaps at this Ca value, driven by the second deformation mode, result in intense wake oscillations and pressure fluctuations (see Fig. 10b2), which in turn increase drag, as observed in Figs. 3 and 4.

The interaction between wake unsteadiness and the flaps response is further illustrated in Fig. 12, where the flow has been conditionally averaged with the wake instantaneous flow fields corresponding to a positive horizontal base pressure gradient (P state), following the procedure proposed by Grandemange et al. (2013b). The conditional averaging is performed by computing the spatial average of u_y inside the recirculation region for each instant. Subsequently, instants associated with a positive spatial average of u_y corresponds to the P wake deflected state. The conditionally averaged flow streamlines and streamwise velocity fluctuations are depicted in Fig. 12 (a, b) for the reference case at $Re \simeq 77000$ and 87000, respectively.

For the reference case at both Re, the P wake state depicts a large recirculation core near the body base at $y/h < 0$, locally decreasing the pressure in that zone. Conversely, the recirculation core on the opposite side is smaller and located further from the base. This wake topology induces a positive horizontal base pressure gradient (P state). The level of fluctuations is greater on the $y/H > 0$ part of the base, as vortices are being shed on that side of the wake. The recirculation regions observed for the P state are very similar to those observed at $\beta = 5°, 10°$ (see Fig. 2d1, d2), validating our analysis of the fluid–structure interaction problem even under yawed conditions.

Since the RSB mode persist in the near wake when the flexible flaps are set for $Ca < 45$ values, conditional averaging can also be performed for this configuration. Fig. 12(c1) illustrates a wake topology similar to that of the reference case. However, both recirculation cores are smaller and located further from the base. On the $y/H < 0$ side, the recirculation core cannot be fully characterized by PIV measurements due to the presence of the flaps. Flexible flaps induce a reduction in the wake asymmetry, resulting in a smaller magnitude of the averaged horizontal base pressure gradient, $|G_y|$ (see Fig. 9a, b). In terms of the flaps' response, we also performed conditional averaging on the flaps deformation to obtain the averaged flaps' deflection for each wake state (see Fig. 12c1). We added two extreme instantaneous flap positions for the selected wake deflected state to illustrate flaps' oscillations amplitude. Under P wake deflected state, the flap on the $y/H > 0$ side oscillates more than the one on the $y/H < 0$ side. Conversely, the mean deflected position for the flap on the $y/H < 0$ side is greater than that for the one in the $y/H > 0$, confirming the proposed fluid–structure interaction mechanism sketched in Fig. 9(c). The near wake features under the tested yaw angles exhibit a similar recirculation region to this P deflected state, so it is expected that the flap response observed at yaw conditions is connected to this mechanism. The large recirculation core placed near the body base at $y/h < 0$, observed for $\beta = 5°$ and 10° in Fig. 2(d1, d2), locally decreases the pressure and forces a more pronounce mean deflected state in the leeward flap (θ_1), as evidenced in Fig. 5(a). On the other hand, the smaller recirculation core, located further from the base, induces a higher level of wake fluctuations, resulting in more oscillations in the windward flap (θ_2), as illustrated in Fig. 5(b). Hence, the second deformation mode is excited at lower values of Ca for the windward flap under $\beta = 5°$ and 10°, since the wake forcing is stronger on that side.

The emergence of this second deformation mode of the flexible flaps induces significant alterations in the near wake topology and leads to higher levels of wake fluctuations, initiating a new fluid–structure coupling between flaps and wake. At $Ca \simeq 53$, the mean deflection of both flaps is inwards (illustrated by the pink solid line in Fig. 12c2), although instantaneous positions of the flaps can reach outward orientations, as depicted by the two selected extreme flap positions (blue and green solid lines) in Fig. 12(c2). This flap response induces notable wake unsteadiness, increasing the level of fluctuations in the shear layers enclosing the recirculation region and introducing new frequency components into the wake (see Fig. 10b2). Such a wake unsteadiness contributes to the observed increase in drag, illustrated in Figs. 3 and 4.

4. Conclusions

We conducted experiments to evaluate the impact of vertical flexible flaps on the turbulent wake behind a simplified model of a vehicle, the squareback Ahmed body. The flexible flaps, covering the vertical trailing edges and having a length of 0.46 H, serve as self-adaptive drag reduction devices, with their effectiveness assessed through wind tunnel experiments under varying conditions of incoming flow velocity (which modifies the plates' flexibility through the corresponding Ca) and its orientation relative to the model (testing different yaw angles, $\beta = 0°, 5°$ and 10°). Three configurations were studied: (1) the baseline case (REF), (2) rigidly mounted flaps of equivalent length (RF), and (3) the flexible flaps (FF).

Our experiments revealed an efficient drag reduction performance of the flexible flaps at low Ca values, regardless of flow orientation. This reduction is achieved through passive inward reconfiguration of the flaps, streamlining the flow separation and reducing the recirculation region size, consequently increasing the base pressure compared to the reference body. Conversely, rigid flaps only marginally reduce drag under aligned conditions (2.5% reduction in C_D), being less effective than the flexible flaps (8.3% reduction). Moreover, the additional surface area of the rigid flaps increases the friction drag and the side forces (C_y) under yawed

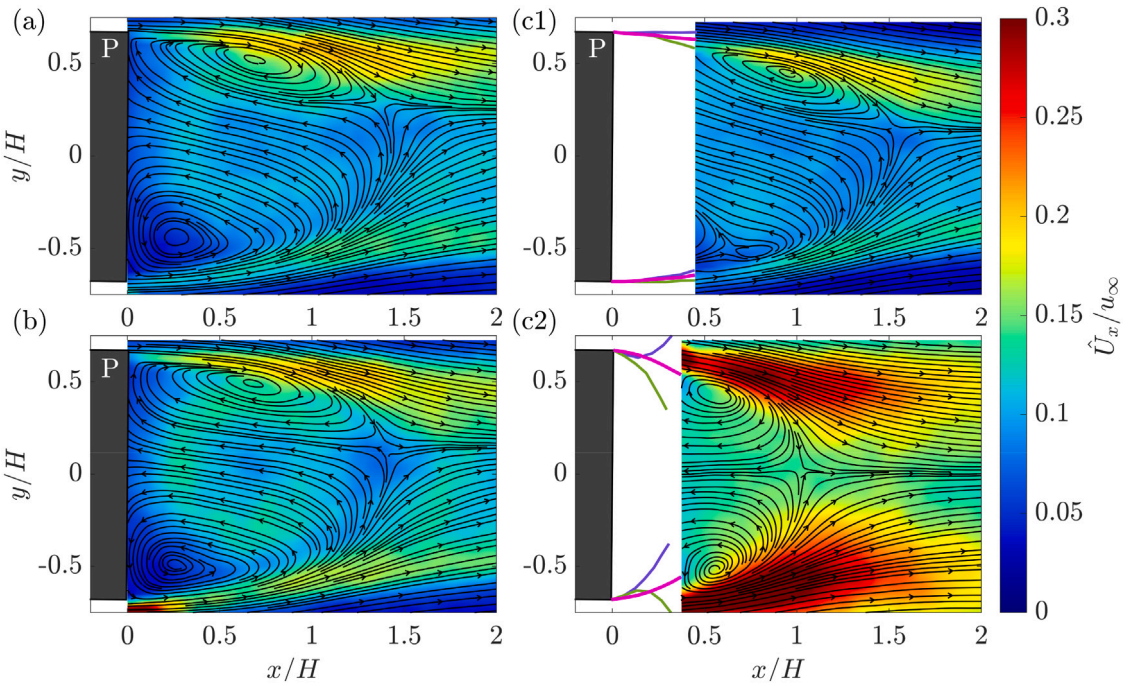

Fig. 12. (a, b) Respective conditionally averaged flow (only P state) at the horizontal plane placed at $z = 0$ for the baseline case at $Re \simeq 77000$ and $Re \simeq 87000$. (c1) Conditionally averaged mean flow (only P state) at the horizontal plane placed at $z = 0$ for the flexible flaps at $Ca \simeq 43$ ($Re \simeq 77000$) (c2) Averaged mean flow at the horizontal plane placed at $z = 0$ for the flexible flaps at $Ca \simeq 53$ ($Re \simeq 87000$). The averaged flow is illustrated by contours of conditionally averaged streamwise velocity fluctuations, $\hat{U}_x$, alongside the corresponding averaged flow streamlines, (U_x, U_y). In (c1, c2), extreme flap deflections are represented in blue and green solid lines, while the averaged flap deflection is depicted in pink solid lines. (For interpretation of the references to color in this figure legend, the reader is referred to the web version of this article.)

conditions. In contrast, flexible flaps effectively counteract the added surface effects, reducing the overall drag even under yaw (also a 7.8% reduction in C_D).

Initially, the flaps deflect inwardly (with an averaged tip deflection angle around $\Theta \simeq 4°$), while oscillating mildly ($\hat{\Theta} \simeq 1°$). As Ca increases, quasi-periodic oscillations with phase differences between flaps emerge (up to $\hat{\Theta} \simeq 25°$), along with different deformation modes. The threshold of instability of the second deformation mode varies with the relative wind orientation, occurring at lower Ca under yawed conditions. The flexible flaps' response, a combination of the first and second deformation modes, accurately captures the instantaneous deflection across all cases.

Further analysis at aligned conditions revealed two different fluid–structure interaction mechanisms between flap deformation and near-wake dynamics. At low Ca, the flaps interact with the reflectional-symmetry breaking (RSB) mode similarly to previous studies, with slow random oscillations of the flaps coupled with the horizontal base pressure gradient (g_y), reflecting bi-stable wake dynamics. However, with the emergence of the second deformation mode, the RSB mode disappears, yielding a symmetric near wake. Yet, intense flap oscillations induce an amplified wake unsteadiness which increases Ahmed body's drag.

These findings suggest potential applications for self-adaptive devices aiming drag reduction for heavy vehicles, while the strong response of flaps in the second deformation mode may offer opportunities for energy harvesting in other contexts.

CRediT authorship contribution statement

J.C. Muñoz-Hervás: Conceptualization, Data curation, Formal analysis, Investigation, Methodology, Visualization, Writing – original draft, Writing – review & editing. **M. Lorite-Díez:** Conceptualization, Data curation, Formal analysis, Investigation, Methodology, Project administration, Resources, Supervision, Validation, Writing – original draft, Writing – review & editing. **C. García-Baena:** Conceptualization, Investigation, Methodology, Software, Writing – review & editing. **J.I. Jiménez-González:** Conceptualization, Formal analysis, Funding acquisition, Investigation, Methodology, Project administration, Resources, Supervision, Writing – original draft, Writing – review & editing.

Declaration of competing interest

The authors declare that they have no known competing financial interests or personal relationships that could have appeared to influence the work reported in this paper.

Data availability

Data will be made available on request.

Acknowledgments

This work is a result of the Projects PDC2021-121288-I00, TED2021-131805B-C21 and TED2021-131805B-C22, financed by the Spanish MCIN/ AEI/10.13039/501100011033/, FEDER, UE, and the European Union NextGenerationEU/PRTR. M.L.D. also acknowledges the support from grant FJC2020-043093-I funded by MCIN/AEI/10.13039/501100011033 and European Union NextGenerationEU/PRTR. Finally, J.C.M.H. acknowledges for the support of the Spanish MECD through FPU20/07261.

Appendix A. Supplementary data

Supplementary material related to this article can be found online at https://doi.org/10.1016/j.jfluidstructs.2024.104124.

References

Abdi, R., Rezazadeh, N., Abdi, M., 2019. Investigation of passive oscillations of flexible splitter plates attached to a circular cylinder. J. Fluids Struct. 84, 302–317.
Ahmed, S.R., Ramm, G., Faltin, G., 1984. Some salient features of the time-averaged ground vehicle wake. SAE Trans. 840300, 473–503.
Barros, D., Borée, J., Cadot, O., Spohn, A., Noack, B.R., 2017. Forcing symmetry exchanges and flow reversals in turbulent wakes. J. Fluid Mech. 829, R1.
Bonnavion, G., Cadot, O., 2018. Unstable wake dynamics of rectangular flat-backed bluff bodies with inclination and ground proximity. J. Fluid Mech. 854, 196–232.
Camacho-Sánchez, J.M., Lorite-Díez, M., Jiménez-González, J.I., Cadot, O., Martínez-Bazán, C., 2023. Experimental study on the effect of adaptive flaps on the aerodynamics of an ahmed body. Phys. Rev. Fluids 8 (4), 044605.
Choi, H., Lee, J., Park, H., 2014. Aerodynamics of heavy vehicles. Annu. Rev. Fluid Mech. 46 (1), 441–468. http://dx.doi.org/10.1146/annurev-fluid-011212-140616.
García de la Cruz, J.M., Brackston, R.D., Morrison, J.F., 2017. Adaptive base-flaps under variable cross-wind. SAE Tech. Pap. 01–7000.
Cui, G.-P., Feng, L.-H., Hu, Y.-W., 2022. Flow-induced vibration control of a circular cylinder by using flexible and rigid splitter plates. Ocean Eng. 249, 110939.
Duell, E.G., George, A.R., 1999. Experimental study of a ground vehicle body unsteady near wake. SAE Trans. 01–0812 (0812), 1589–1602.
European Environment Agency, 2021. Greenhouse Gas Emissions from Transport in Europe. Technical Report.
Evrard, A., Cadot, O., Herbert, V., Ricot, D., Vigneron, R., Délery, J., 2016. Fluid force and symmetry breaking modes of a 3D bluff body with a base cavity. J. Fluids Struct. 61, 99–114.
García-Baena, C., Camacho-Sánchez, J., Lorite-Díez, M., Gutiérrez-Montes, C., Jiménez-González, J., 2023. Drag reduction on a blunt body by self-adaption of rear flexibly hinged flaps. J. Fluids Struct. 118, 103854.
García-Baena, C., Jiménez-González, J.I., Gutiérrez-Montes, C., Martínez-Bazán, C., 2021b. Numerical analysis of the flow-induced vibrations in the laminar wake behind a blunt body with rear flexible cavities. J. Fluids Struct. 100, 103194.
García-Baena, C., Jiménez-González, J.I., Martínez-Bazán, C., 2021a. Drag reduction of a blunt body through reconfiguration of rear flexible plates. Phys. Fluids 33 (4), 045102. http://dx.doi.org/10.1063/5.0046437.
Grandemange, M., Cadot, O., Courbois, A., Herbert, V., Ricot, D., Ruiz, T., Vigneron, R., 2015. A study of wake effects on the drag of ahmed's squareback model at the industrial scale. J. Wind Eng. Ind. Aerodyn. 145, 282–291.
Grandemange, M., Gohlke, M., Cadot, O., 2013a. Bi-stability in the turbulent wake past parallelepiped bodies with various aspect ratios and wall effects. Phys. Fluids 25 (9), 095103.
Grandemange, M., Gohlke, M., Cadot, O., 2013b. Turbulent wake past a three-dimensional blunt body. Part 1: Global modes and bi-stability. J. Fluid Mech. 722, 51–84. http://dx.doi.org/10.1017/jfm.2013.83.
Gutierrez, W.T., Hassan, B., Croll, R.H., Rutledge, W.H., 1995. Aerodynamics overview of the ground transportation systems (GTS) project for heavy vehicle drag reduction. Technical Report, Sandia National Lab (SNL-NM), Albuquerque, NM (USA).
Haffner, Y., Borée, J., Spohn, A., Castelain, T., 2020. Mechanics of bluff body drag reduction during transient near-wake reversals. J. Fluid Mech. 894, A14.
Hedrick, T.L., 2008. Software techniques for two-and three-dimensional kinematic measurements of biological and biomimetic systems. Bioinspiration Biomim. 3 (3), 034001.
Howell, J., Passmore, M., Tuplin, S., 2013. Aerodynamic drag reduction on a simple car-like shape with rear upper body taper. SAE Int. J. Passeng. Cars Mech. 6 (2013-01-0462), 52–60.
Hucho, W.H., Sovran, G., 1993. Aerodynamics of road vehicles. Annu. Rev. Fluid Mech. 25 (1), 485–537.
Khalighi, B., Zhang, S., Koromilas, C., Balkanyi, S., Bernal, L.P., Iaccarino, G., Moin, P., 2001. Experimental and computational study of unsteady wake flow behind a bluff body with a drag reduction device. SAE Trans. 01–1042 (1042), 1209–1222.
Kunze, S., Brücker, C., 2012. Control of vortex shedding on a circular cylinder using self-adaptive hairy-flaps. C. R. Mec. 340 (1–2), 41–56.
Lorite-Díez, M., Jiménez-González, J.I., Pastur, L., Cadot, O., Martínez-Bazán, C., 2020a. Drag reduction on a three-dimensional blunt body with different rear cavities under cross-wind conditions. J. Wind Eng. Ind. Aerodyn. 200, 104145.
Lorite-Díez, M., Jiménez-González, J.I., Pastur, L., Martínez-Bazán, C., Cadot, O., 2020b. Experimental sensitivity analyses of modes to blowing at the base of a 3D bluff body. J. Fluid Mech. 883, A53.
Mao, Q., Zhao, J., Liu, Y., Sung, H.J., 2022. Drag reduction by a flexible hairy coating. J. Fluid Mech. 946, A5.
McArthur, D., Burton, D., Thompson, M., Sheridan, J., 2018. An experimental characterisation of the wake of a detailed heavy vehicle in cross-wind. J. Wind Eng. Ind. Aerodyn. 175, 364–375.
National Research Council, 2010. Technologies and Approaches to Reducing the Fuel Consumption of Medium-And Heavy-Duty Vehicles. National Academies Press.
Rao, S.S., 2011. Mechanical Vibrations.
Roshko, A., 1993. Perspectives on bluff body aerodynamics. J. Wind Eng. Ind. Aerodyn. 49 (1-3), 79–100.
Urquhart, M., Varney, M., Sebben, S., Passmore, M., 2021. Drag reduction mechanisms on a generic square-back vehicle using an optimised yaw-insensitive base cavity. Exp. Fluids 62 (12), 1–21.
Varney, M., Passmore, M., Gaylard, A., 2018. Parametric study of asymmetric side tapering in constant cross wind conditions. SAE Int. J. Passeng. Cars Mech. 11 (06-11-03-0018), 213–224.
Wieneke, B., 2015. PIV uncertainty quantification from correlation statistics. Meas. Sci. Technol. 26 (7), 074002.
Wood, R.M., Bauer, S.X., 2003. Simple and low-cost aerodynamic drag reduction devices for tractor-trailer trucks. SAE Tech. Pap. 01–3377 (3377), 143–160.